

# Simulations of Kelvin-Helmholtz Instability with $Ri = 0.10$

Tyler Mitchell  
Nicholas J. Nelson  
Anthony Rasca  
Don Schmit

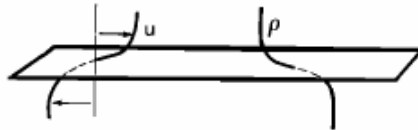
May 6, 2009

## 1 Introduction

One way in which vertical mixing can occur in the atmosphere is by Kelvin-Helmholtz instabilities between two stably stratified layers. The onset of Kelvin-Helmholtz instabilities is characterized by the iconic billow formation, which can sometimes be visible in cloud layers. A cartoon picture of the formation and evolution of Kelvin-Helmholtz billows in laboratory experiments is shown in Fig. 1, which describes many elements of the overall evolution of our simulations. These instabilities and their ability to generate turbulence have been widely researched, but are still poorly parameterized and thus still capable to revealing new information.

This paper analyzes the data produced from the Julian-Werne “Triple” code simulating Kelvin-Helmholtz instabilities using a Richardson number of  $Ri = 0.10$ . Two other groups ( $\alpha$  and  $\sigma$ ) use  $Ri = 0.05$  and  $Ri = 0.20$ , respectively, and their results will be compared with ours. We performed three simulations: 2D and 2D direct numerical simulation (DNS) and a 3D large-eddy simulation (LES). Data analysis will focus on observing the flow during moments of maximum kinetic energy and vorticity, in addition to the transition from a laminar to turbulent flow. Comparing DNS and LES data with respect to flow evolution and morphology will also be a focus of the data analysis.

STAGE 0, PARALLEL STRATIFIED FLOW



STAGE 1, K-H INSTABILITY AND GROWTH OF BILLOWS

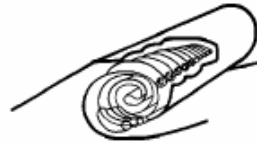


STAGE 2,

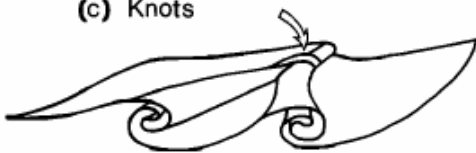
(a) Subharmonic vortex pairing



(b) Convective Rolls



(c) Knots



(d) Tubes



STAGE 3, UNKNOWN

STAGE 4, SECONDARY BILLOWS AND UNIDENTIFIED STRUCTURES IN BILLOWS  
-CHAOS ?



Figure 1: Schematic diagrams of various stages of the evolution of billows in Kelvin-Helmholtz instabilities highlighting the formation of the initial billows and various secondary instabilities as the simulation moves towards well-mixed turbulence (from Thorpe, S.A., 1987, "Transitional phenomena and the development of turbulence in stratified fluids", Journal of Geophysical Research, C5, 5231-5248).

## 2 Numerical Simulation Parameters

Simulations for the DNS and LES codes were run on a LASP 243-node supercomputer, both using Richardson and Reynolds numbers of  $Ri = 0.10$  and  $Re = 1600$ , respectively. New volume files were written every 100 time steps and plane files every 50 time steps. Output files include data on vorticity, velocity and temperature for each spatial direction.

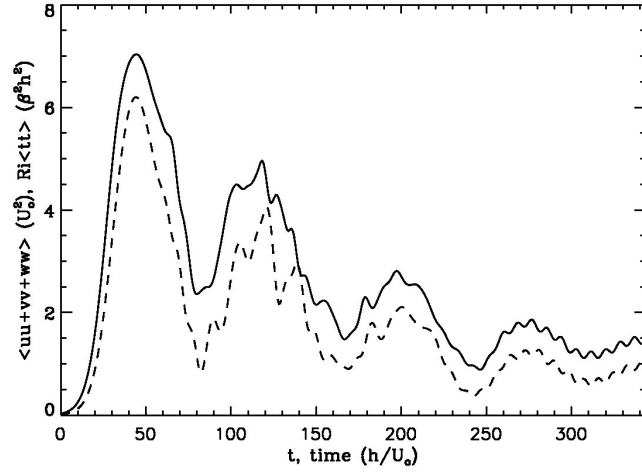
The DNS run was split into 2D and 3D cases. The DNS cases were first run with a 2D case partly to ensure computations were being performed correctly without spending much time testing with a 3D case, but also to allow comparisons between both cases. We used 30000 time steps on a 600x600 ( $z$  by  $x$ ) grid, carrying the simulation out to a time of about 300 in fluid crossing times. The 2D case was computationally inexpensive, requiring only 50 processors. The 3D case for the DNS run was performed with a 600x150x600 ( $z$  by  $y$  by  $x$ ) grid and used 9000 time steps to reach a final time of 160, using 300 processors.

The LES run did not require as high of a resolution as the DNS cases, so the grid was reduced by a factor of three in each dimension to 200x50x200. The simulation ran to a time of 147, using 3000 time steps. We used 200 processors for this case. The low resolution required for the LES case made it much quicker to compute even with the additional expense of computing the sub-grid scale viscosities at each point at every time step.

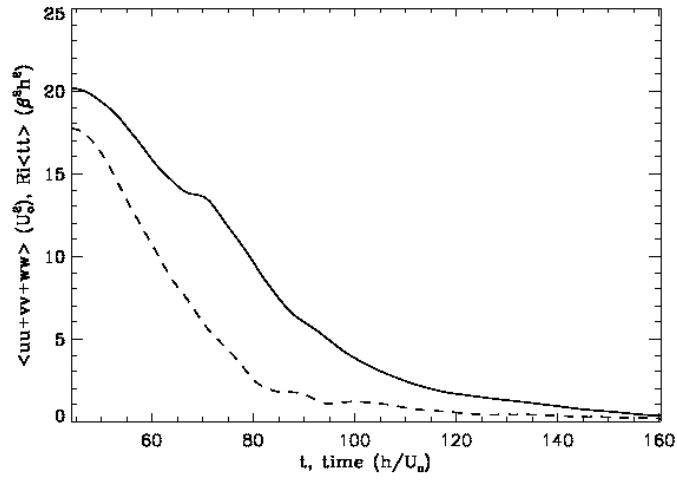
## 3 Total Kinetic Energy and Maximum Vorticity

Total kinetic and potential energy plots for all three cases are displayed in Fig. 2. KE/PE plots for all three runs look very similar previous to a time of about 45. This is because the 3D simulation is basically 2D up until this point. Comparisons between the LES and DNS cases also reveal similarities, but at a level where they can only be discerned through close inspection. The energies increase from zero, to a maximum at about  $t = 45$ . It is interesting to note that the energies of the lower Richardson number of group  $\alpha$  peaked earlier at about  $t = 30$  and that the higher Richardson number case of group  $\sigma$  peaked later at about  $t = 80$ .

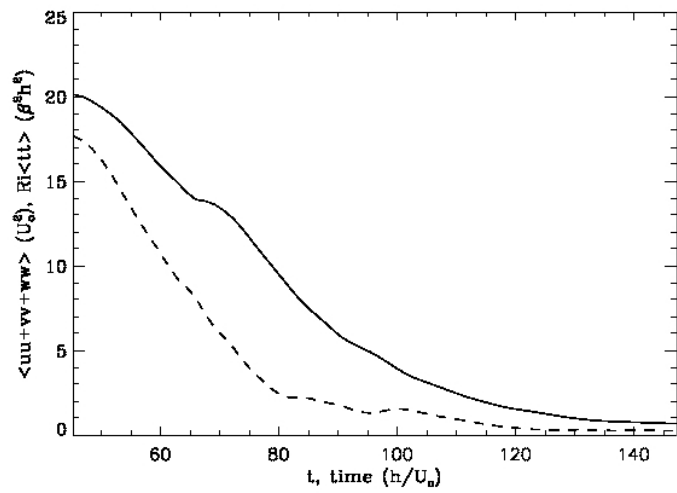
Initially the 2D case's energy traces look like that of the 3D DNS and LES cases, but only until  $t = 80$ . After this point the 3D cases continue to decay asymptotically to zero. The 2D case only decays to a value of about a third of the maximum value attained. From here onward the energies associated with the 2D case show large oscillations with a period of about 60-70 crossing times. Overall, the energies slowly decay, but do not reach zero within our time domain. Also note that the maximum values obtained for PE and KE for the 2D case are much smaller than the maximums attained in the 3D cases. Dr. Joe Werne states that this is due to a normalization factor, set internally in Triple, that allows for the comparison of runs with different resolutions. It should not effect the behavior of the run, as it is simply a rescaling.



(a)



(b)



(c)

Figure 2: Total kinetic (solid lines) and potential (dashed lines) energy plots for (a) the 2D LES case, (b) 3D DNS case, and (c) 3D LES case.

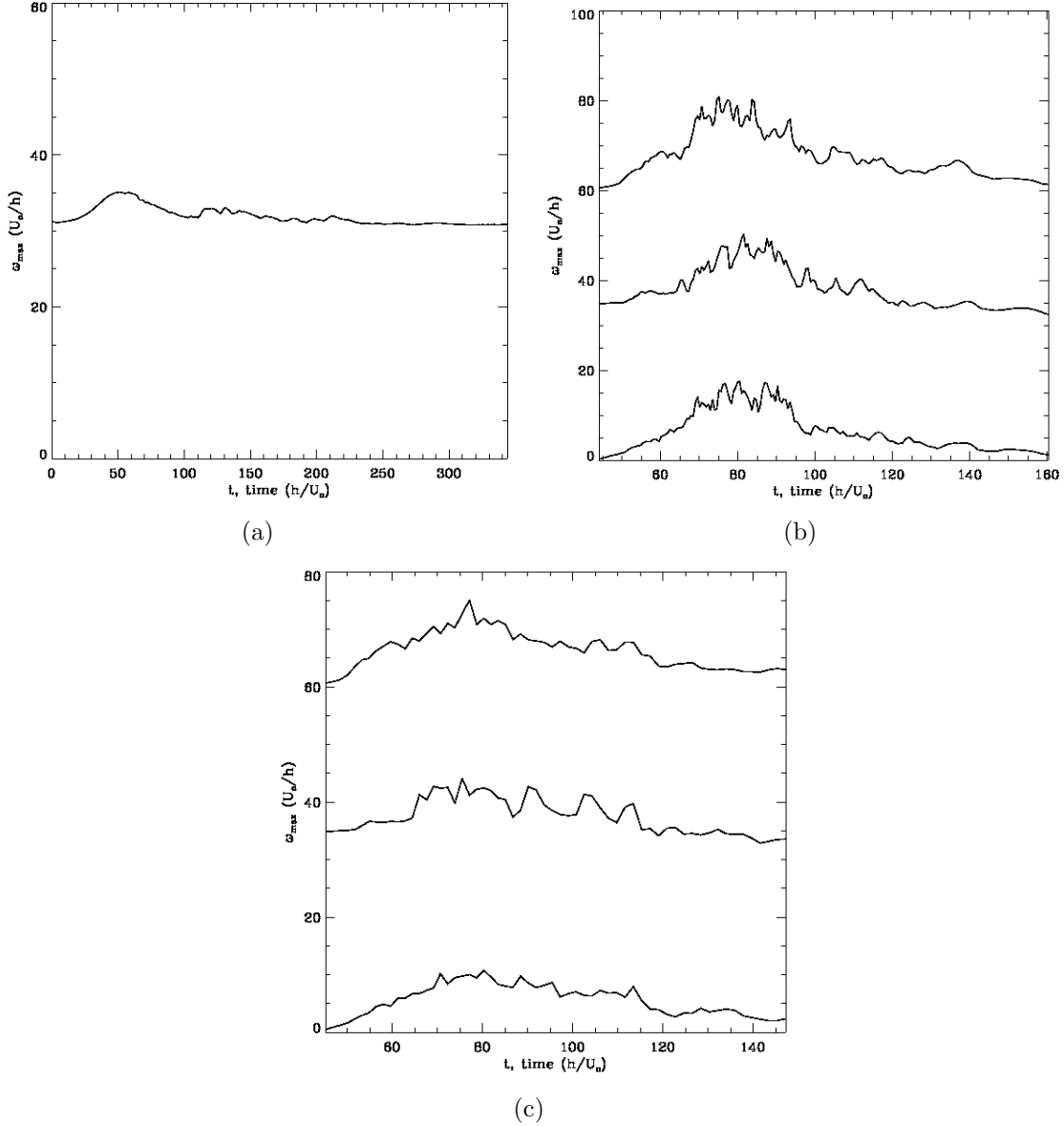


Figure 3: Point-wise maximum vorticity plots for (a) the 2D LES case, (b) 3D DNS case, and (c) 3D LES case. For (b) and (c), lines are, from top to bottom,  $\omega_z + 60$ ,  $\omega_y + 30$ , and  $\omega_z$  with offsets added for visual clarity.

As with the energy plots, the vorticity plots of the 3D cases look very similar (Fig. 3), with the main exception being that the DNS case has many more small scale variations than the LES case. According to Werne, this is due to the fact that the vorticity is a derivative quantity and is highly dependent on the resolution of the problem. Therefore, the reduced resolution of the LES case cannot capture the small scale variations present in the DNS case. In both, the  $y$ -vorticity is non-zero at the beginning of the simulation, whereas the  $x$  and  $z$  components are zero until about  $t = 40$ , when the vortex begins to stretch and bend and the turbulence begins distributing the vorticity in the other two components. The 2D case has only the  $y$  component of vorticity and qualitatively it behaves much like the 3D cases, but it peaks much sooner than the 3D cases. This occurs at  $t = 45$ , instead of  $t = 80$  for the 3D cases.

## 4 2D Time Evolution

Many aspects of the time evolution of the 2D case can be best seen by looking at the evolution of vorticity. In the 2D case, there is no mechanism for stretching vortex tubes, which inhibits the cascade of vorticity to progressively smaller scales compared with the behavior of the 3D cases. Figure 4 shows snapshots of the  $y$ -component of vorticity at six times in the simulation. Unlike the 3D cases, the 2D case was run from  $t = 0$ , so we can see the onset of the primary Kelvin-Helmholtz instability and the formation of the large roll structure. After the formation of the billow, the simulation shows some 2D turbulence on the ends of the billow and above and below the billow, but the core of the billow remains in solid body rotation as evidenced by a nearly constant value (shown in purple) at the center of the billow. Through the turbulent phase of the simulation the billow moves slowly towards the right of the box. When the simulation reaches a steady-state at late times, the billow has moved almost half of the length of the domain. This is very similar to the result from the  $Ri = 0.2$  group, where their 2D billow also fell into a rotating steady state.

One interesting aspect of the 2D turbulence realized in this simulation is the fact that unlike the 3D cases, the 2D cases never produces any locations in the simulation where the vorticity changes sign. Initial vorticity at each point is zero or in the positive  $y$  direction. Interestingly, no negative values of vorticity are realized in this simulation. One explanation for this is that since there are no other components of vorticity realized in this simulation, it is impossible to turn vortex structures. Negative vorticity in the 3D cases is only produced when vortexes are turned in the  $x$  or  $z$  directions and then continue to be turned until they create negatively signed  $y$  vorticity.

Looking at the equation for vorticity in 2D we see that

$$\partial_t \omega + (u \partial_x + w \partial_z) \omega = \nu \nabla^2 \omega. \quad (1)$$

Since the diffusion operator cannot cause a change in sign of the vorticity, let us consider

$$\partial_t \omega = - (u \partial_x + w \partial_z) \omega. \quad (2)$$

Since there is no non-linearity in  $\omega$  in this equation, its time dependence at any point can be given as a simple growing or decaying exponential, which cannot change sign. Therefore since the simulation began with no negative values of  $\omega$  in the initial conditions, it is impossible to develop negative values at later times.

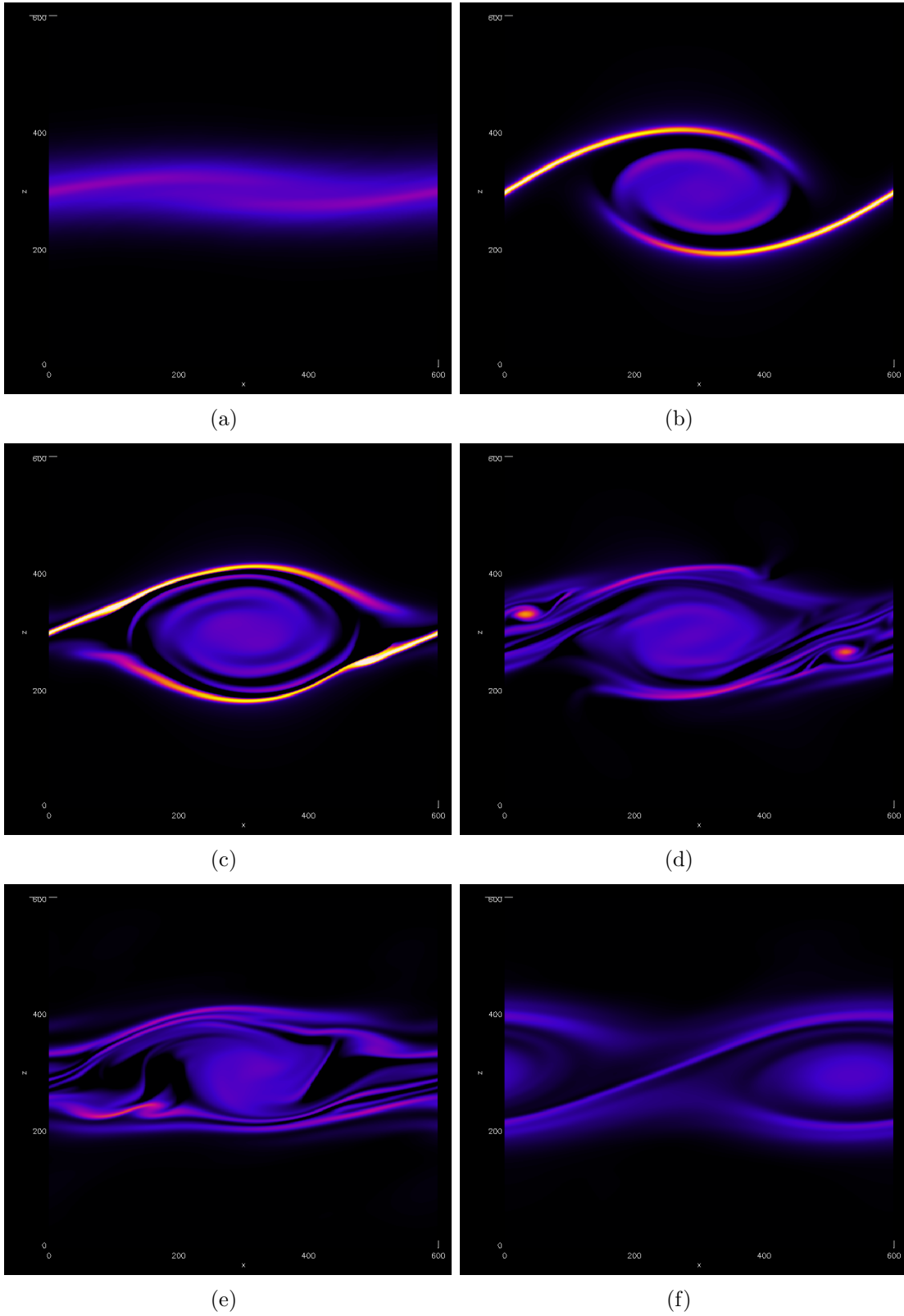


Figure 4: Time evolution of the 2D case shown in the  $y$ -component of vorticity with color representing the value of the  $y$ -component of vorticity going from small values in black and dark purples to large values in pink and white.

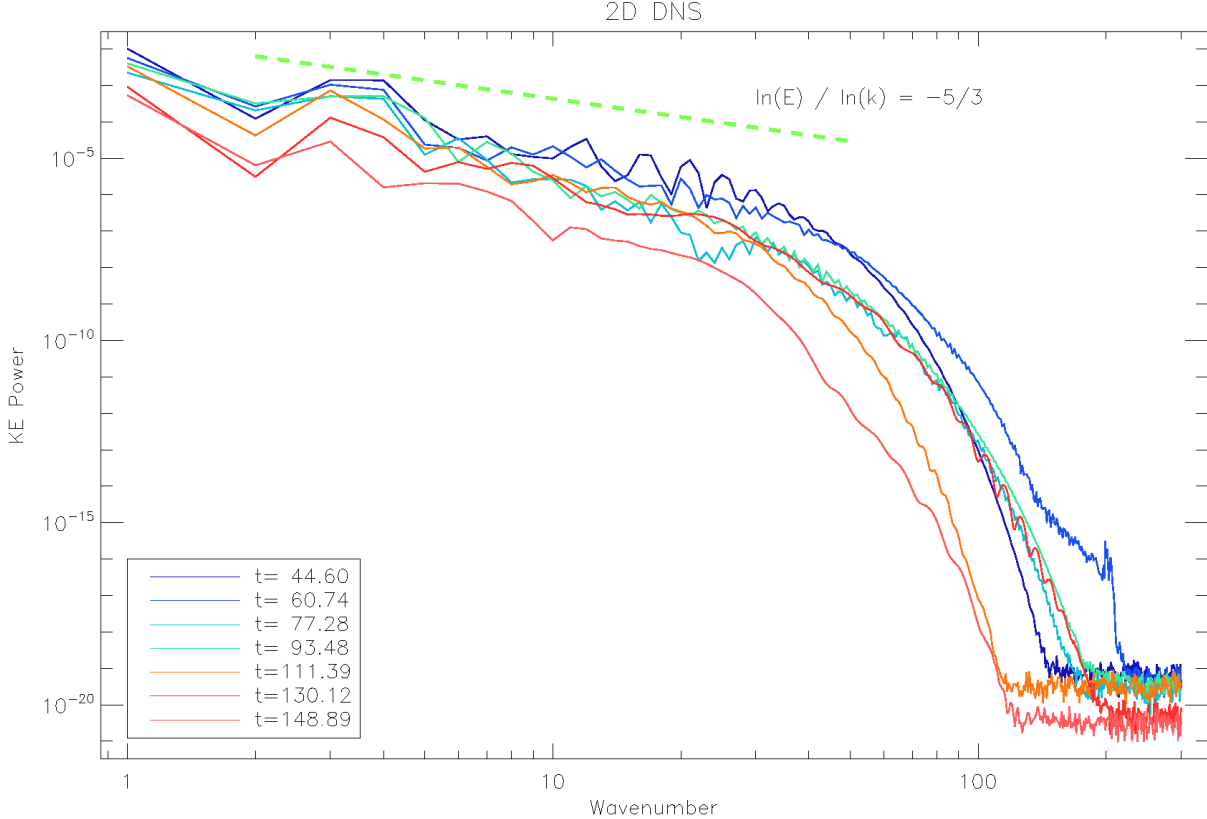


Figure 5: Spectra in the  $x$  direction at the mid-plane, averaged over the  $y$  direction at a single instant of the 2D case at various times, where times move from early to late as shown by a move from blue to red in line color.

The spectra of the 2D case, shown in Fig. 5, demonstrates several interesting properties of this solution. First, the spectra exhibit a Kolmogorov spectra through an inertial range from about  $k = 3$  to  $k = 20$ . This is interesting in that, as noted previously, the turbulence has some unphysical properties such as the inability to produce negative vorticity, yet still develops a  $-5/3$  slope. This is an indication that while a Kolmogorov spectrum does indicate turbulence, caution must be taken not to use the  $-5/3$  slope as evidence for the correctness of the physical model. The spectra in Fig. 5 also show that the dissipation range moves to progressively smaller wavenumbers as the simulation advances in time, which would indicate a monotonic decrease in the Reynolds at a given wavenumber with time. This will be compared to the behavior of the 3D cases later in this paper.

## 5 3D Direct Numerical Simulation

### 5.1 Evolution of Vorticity

Figure 6 shows the time evolution of the 3D DNS case in volume renderings of the  $y$ -component of vorticity at various times. In this case, as in the 2D case, the onset of turbulent behavior occurs at the edges of the billow in the area between the core and the sheets of high vorticity at the edge of the billow. The core stays in solid-body rotation for only about one rotation before turbulence spreads inward and disrupts it, as opposed to multiple rotations in experiment with  $Ri = 0.05$  and the immediate onset of turbulence in the core for the  $Ri = 0.2$  case. Here the billow becomes a layer of turbulence, confined by the mean stratification to an area that fills the domain in  $x$  and  $y$  but covers roughly a third the total domain in  $z$ . This turbulence moves to progressively smaller scales, as expected, until the flow again approaches a laminar state near the end of the simulation. Unlike in the 2D case, here the turbulence does produce negatively values of  $\omega_y$ , however there is still a strong preference toward positive values (shown in blues and greens) over negative values (reds and yellows).

While Fig. 6 shows many aspects of the time evolution of the simulation, by rendering enstrophy we can capture the effects of  $\omega_x$  and  $\omega_z$  as well. Figure 7 shows volume renderings of enstrophy at three times, from a perspective that is rotated about  $30^\circ$  to the right from that of Fig. 6 in an attempt to show some of the variation in  $y$  as well as the variation in  $x$  and  $z$ . Here the values of enstrophy clearly grow as time passes and visible structures move to progressively smaller scales. Figure 5b also shows some hints of tube-like structures, as seen near the right edge of the figure.

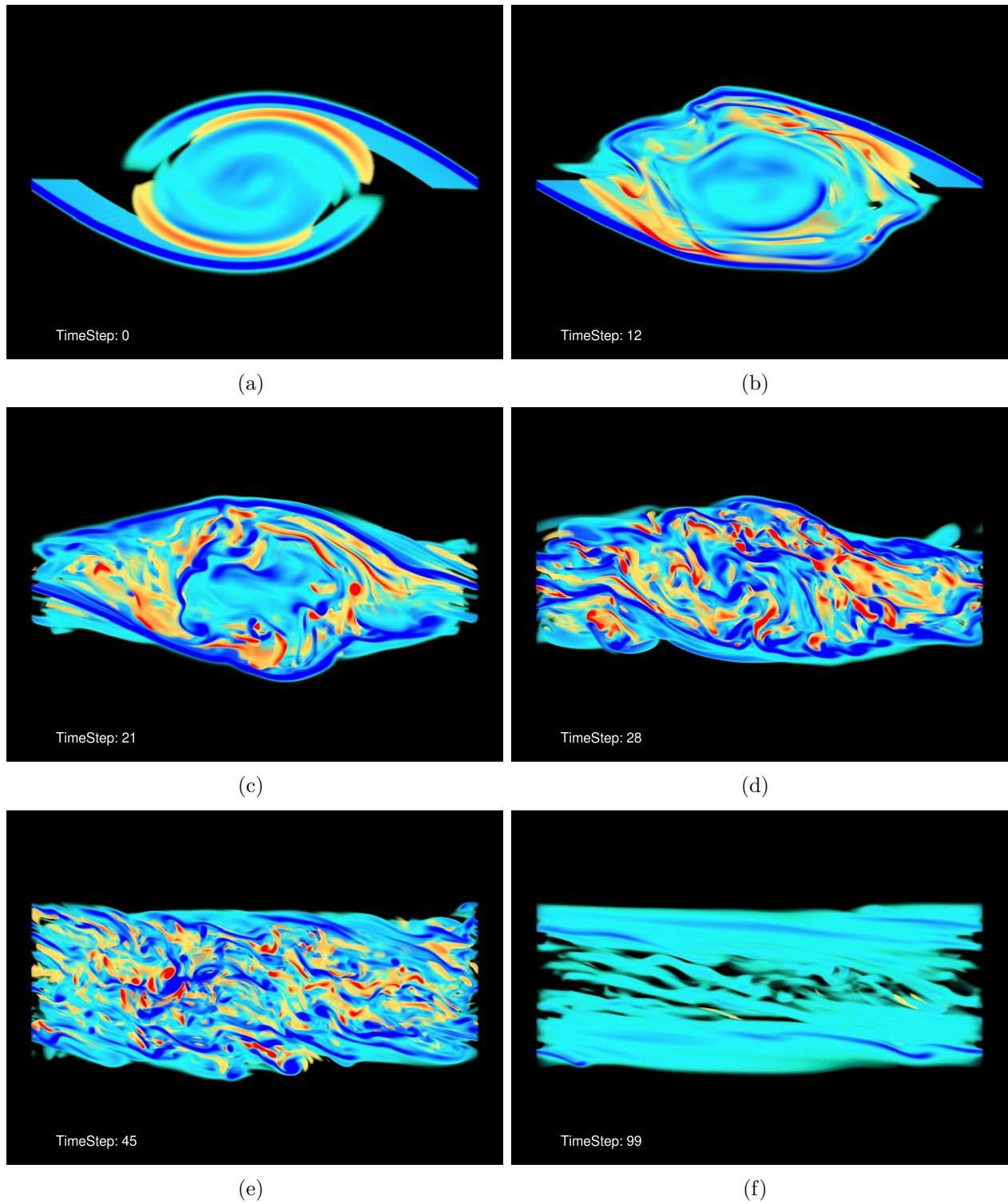
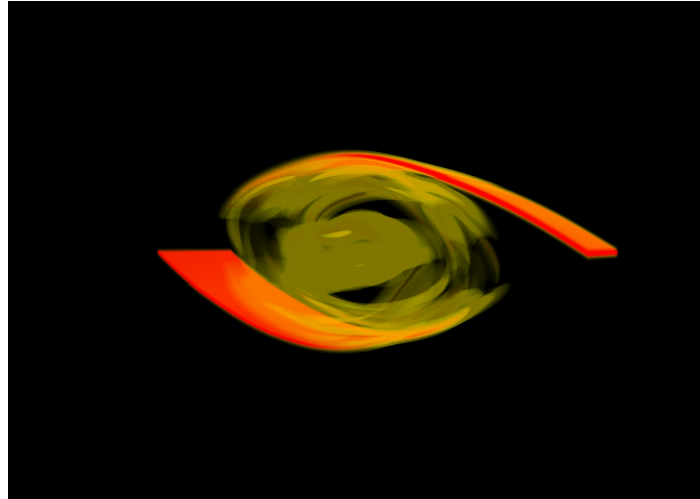
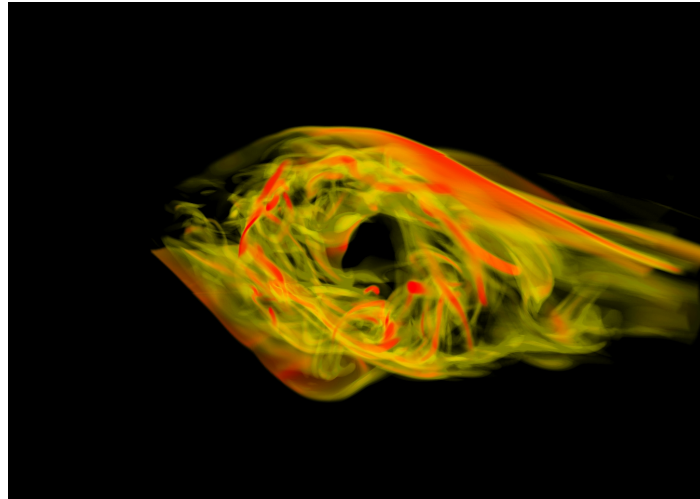


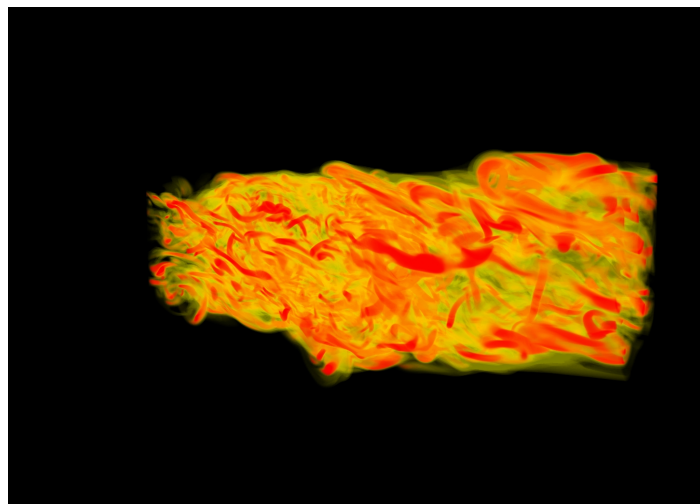
Figure 6: Volume renderings of the  $y$ -component of vorticity at various times during the 3D DNS case where color goes from reds and yellows (negative values of  $\omega_y$ ) to greens and blues (positive values).



(a)



(b)



(c)

Figure 7: Volume renderings of enstrophy where color goes from small values in yellow to large values in red as seen from an angle approximately  $30^{\text{deg}}$  to the right from the viewpoint shown in Figs. 4 and 6.

## 5.2 Spectra Analysis and Probability Distribution Function

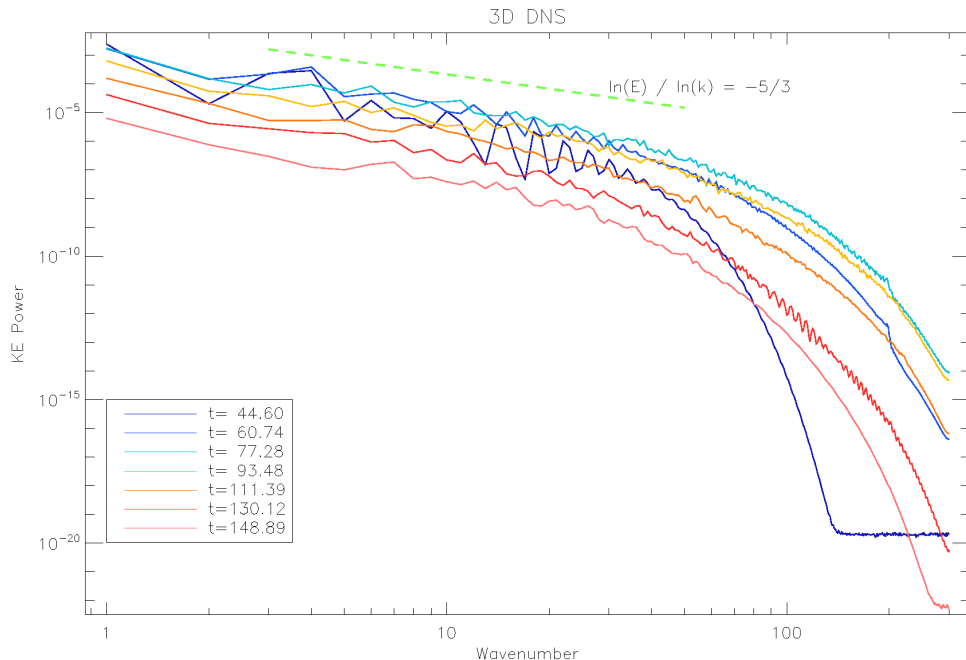


Figure 8: Kinetic energy spectra taken in the  $x$  direction at the mid-plane, averaged over the  $y$  direction at a single instant in time of the 3D DNS case at various times moving from early times in blue to late times in red.

Unlike the 2D case, the spectra of the 3D DNS case shown in Fig. 8 show several features that match our physical intuition about this situation. First the spectra after  $t = 44.60$  exhibit the expected  $-5/3$  scaling from  $3 \lesssim k \lesssim 30$ . The values at  $k = 1$  are monotonically decreasing in time, which indicates that the large scale motions are effectively and simply diffusing away. This reinforces the idea that a cascade of turbulent motions has the effect of enhancing diffusion on large scales. Power in the kinetic energy at small scales first grows until about  $t = 93$  and then decreases, which can be interpreted as an initial filling of the turbulent spectra near the onset of turbulence followed by decay as viscosity drains the kinetic energy from the system, which was only driven initially and then left to decay. The spectra at early times also show a pronounced sawtooth effect at low wavenumbers, which can be attributed to the presence of the billow, which is essentially a top-hat function in kinetic energy at early times whose Fourier transform would produce a sinc function in wavenumber space.

For the 3D DNS case, we also computed probability distribution functions (PDFs) for  $u$  and  $\omega_y$ , shown in Fig. 9. Figure 9 shows the evolution of these PDFs over the course of the simulation. The time evolution of the PDF for  $\omega_y$ , shown in Fig. 9a, shows the development of the turbulent cascade over time. At early times the main feature of the PDF is the second peak at  $\omega_y = 1$ , which is caused by the laminar development of the billow. As the simulation becomes more turbulent the width of the PDF grows and it retains a preference for positive values of  $\omega_y$ , as discussed previously. At late times, the PDF becomes narrower and steeper since diffusion operates most effectively on the large values of  $\omega_y$  that occur infrequently. Fi-

nally at late times, the PDF becomes dominated by the asymmetric shoulder on the positive side, which can be maintained by the more laminar shear at late times.

The PDFs of  $u$ , shown in Fig. 9b, has four broad low peaks at early times with two pairs of peaks centered at  $\pm 1$ . Since the initial conditions had  $|u| \leq 1$  for all points in the domain, the peaks centered above  $u = 1$  and below  $u = -1$  must be due to the billow, which appears to cause a speed up in the fluid above and below the billow at early times. As the simulation progresses, these peaks become narrower and taller and move towards  $\pm 1$  until by late times they have merged to form single peaks at  $\pm 1$ . This indicates that the regions above and below the billow undergo diffusive processes which tend to cause the entire top and bottom of the domain to move at uniform velocities with  $u = \pm 1$ , respectively. Also at late times we see the growth of a low, broad peak centered on zero which is consistent with the center third of the domain in  $z$  being well mixed so that it also moves at uniform velocity with  $u = 0$ . The width of this center peak indicates that the mixing is not yet totally complete. If this simulation were to continue, we would expect the peaks at  $\pm 1$  to continue to move to  $\pm 1$  due to the boundary conditions while the peak at  $u = 0$  should eventually broaden and shrink as the system develops a linear gradient in velocity due to viscous processes.

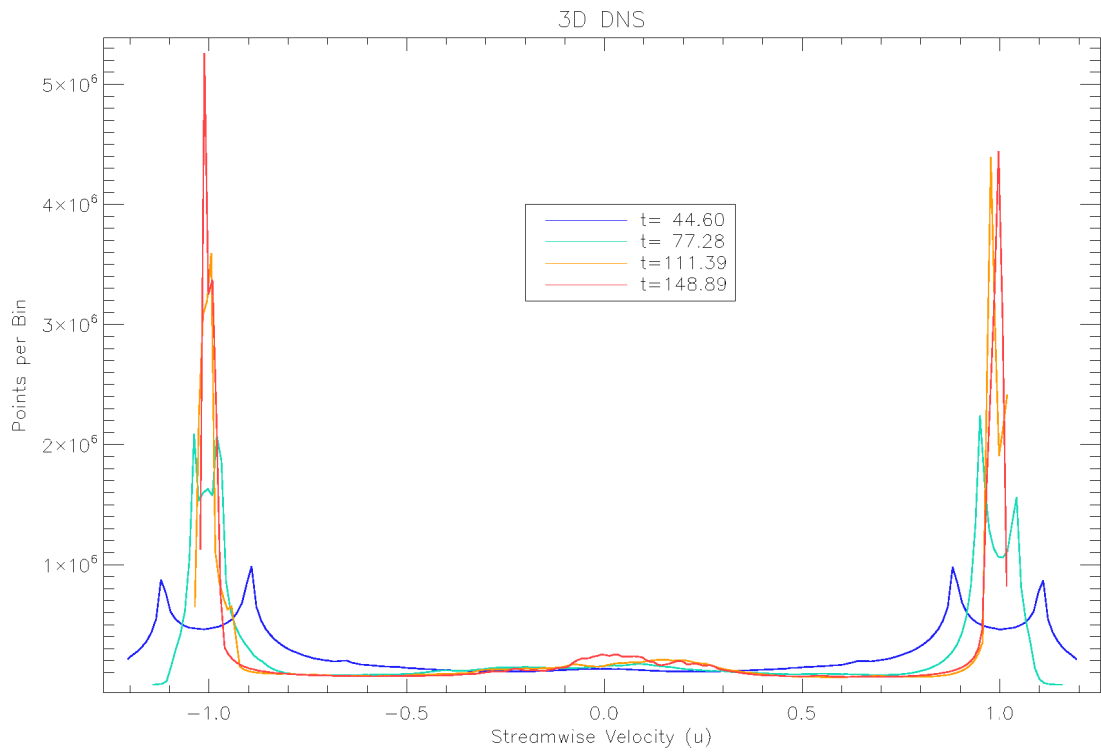
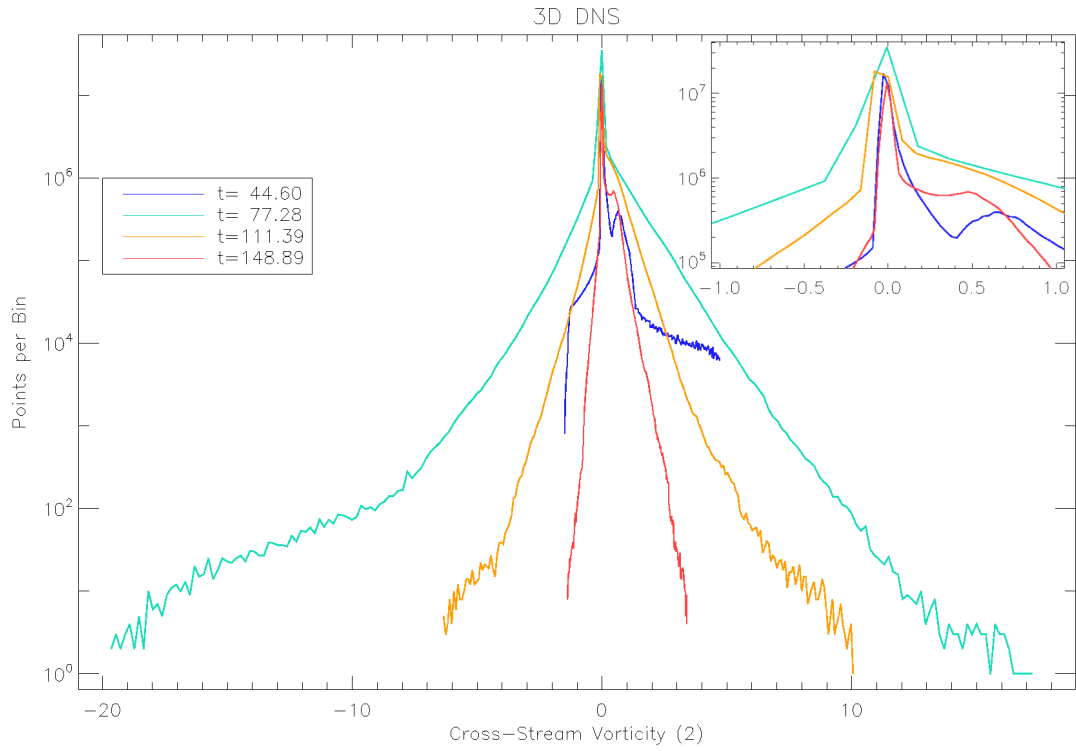


Figure 9: PDFs for the 3D DNS case for (a)  $\omega_y$  and (b)  $u$  at four times in the evolution of the cases. Note that for both plots at all times the total number of points was  $5.409 \times 10^7$  and all PDFs used 200 bins.

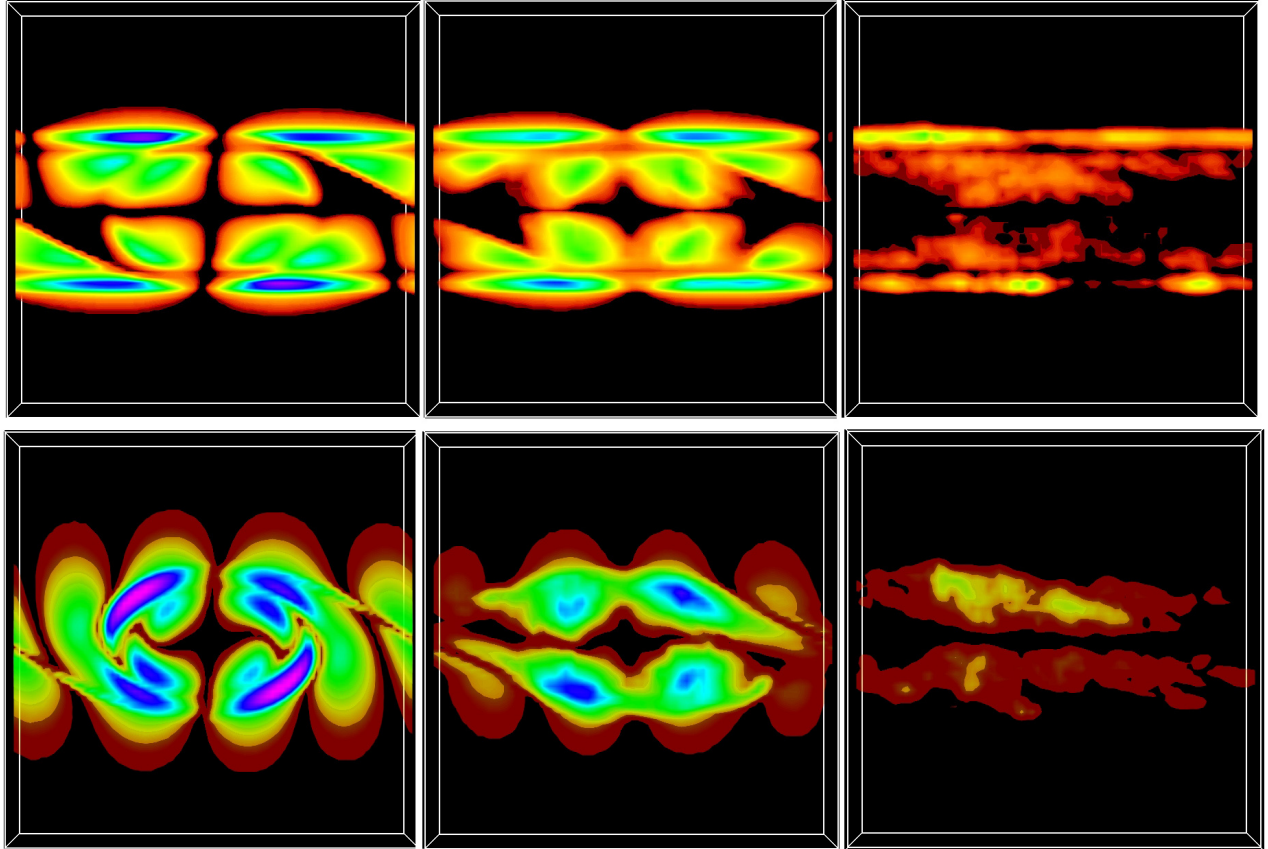


Figure 10: Shear production,  $\text{Ri}\langle w\theta \rangle$ , (top row) and buoyancy production,  $-\langle uw \rangle \partial_z \bar{U}$ , (bottom row) in the 3D DNS, where values are increasing from zero in black to intermediate values in browns and greens to the largest values in blues and purples. Columns left to right represent data at times 44.6, 66.2, and 93.5.

### 5.3 Analysis of Shear and Buoyancy Production

The shear and buoyancy production terms represent a means of understanding the onset and dissipation of the instability. KH is, in the most basic sense, the interplay of shear which attempts to delaminarize the flow while buoyancy struggles to maintain the stratification. It is buoyancy which provides the potential energy in the instability. The buoyancy and shear production are given by  $\text{Ri}\langle w\theta \rangle$  and  $-\langle uw \rangle \partial_z \bar{U}$ , respectively. Figure 10 shows the visualization of the shear and buoyancy in the central  $x$ - $z$  plane. The color schemes are uniform with the minimum represented by red and the maximum by blue. The first column of images represents the initialization state of the 3D DNS model where the billow is first starting to form. The shear and buoyancy terms are largest in distinct regions. Shear production displays an outline of the billow, but it is dominated by the shear layers above and below the billow. These layers are most likely enhanced by the derivative term in the  $z$  direction. The two-fold symmetry in the shear images is interesting and unexpected. Inside the billow, the low shear areas correspond to the locations where  $x$  velocity (horizontally aligned region) and  $z$  velocity (vertically aligned region) approach zero. We do not know how to account for the fact that the vertically aligned, low shear region also occurs in the bounding shear layers.

The initial buoyancy production is concentrated within the billows. The buoyancy term is related to the vertical momentum flux so it is not surprising that billow is highlighted. In the laminar flow, we would not expect to see significant vertical velocities, but in the billow vertical mixing is prevalent.

As time progresses the regions of enhanced shear and buoyancy production both shrink. In both the first and second columns, the billow core does not show strong production in either term. Data dump 20 is slightly before the core goes turbulent and the slow onset of turbulence is most likely a result of the low value of the production terms. After the breakup of the billow, shear and buoyancy both decay, however buoyancy production decays faster, and rather than decaying into two isolated layers as shear does, buoyancy seems to clump more. The fast decay of buoyancy echoes the fact that the decay of the instability leads back into stable stratification.

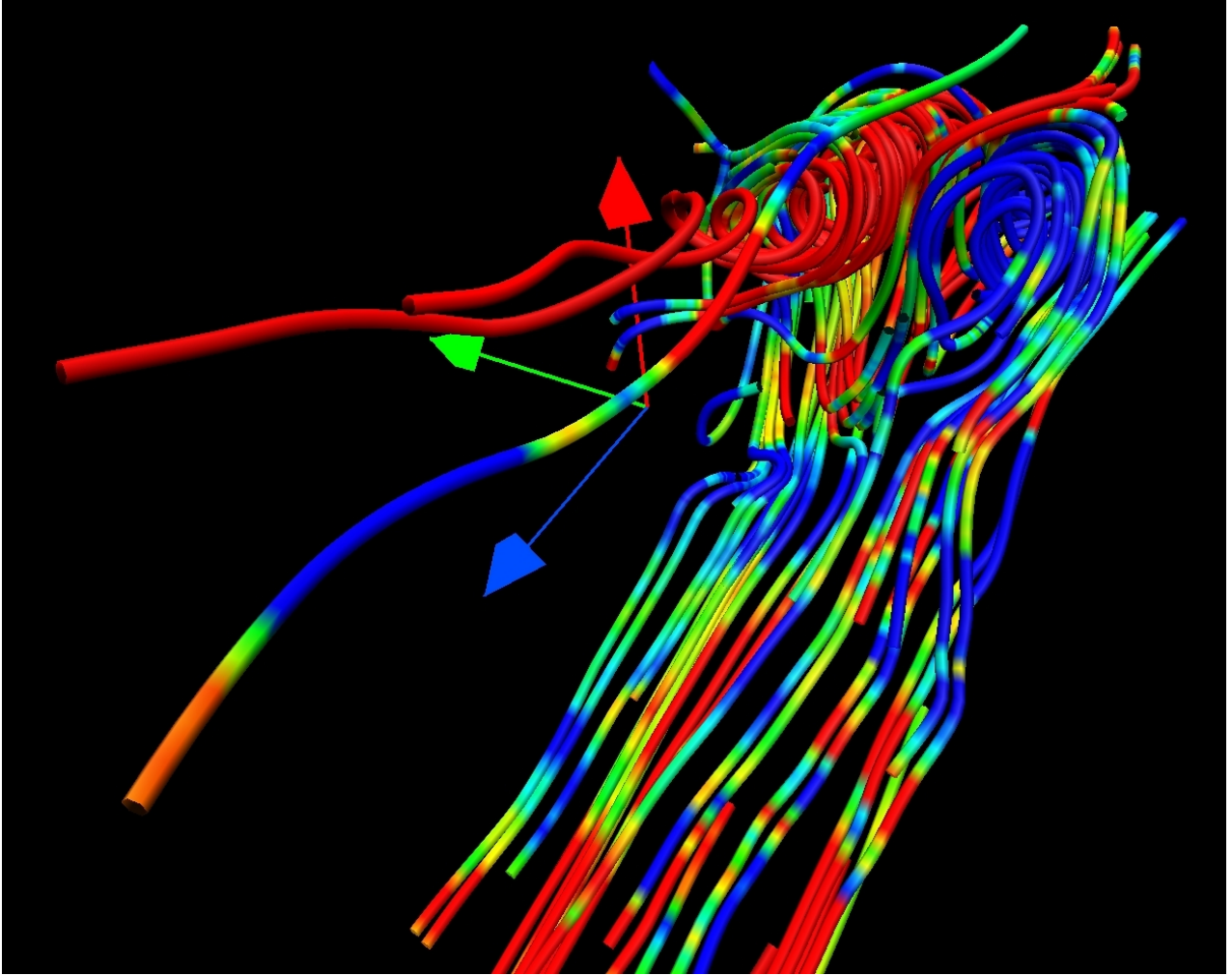


Figure 11: Streamline tracings colored by  $\omega_x$  going from negative values in blue to zero in green to positive values in red, showing a pair of strong vortex structures at  $t \approx 65$ . Here the point of view, as indicated by the axis in the background (red =  $\hat{z}$ , green =  $\hat{y}$ , blue =  $-\hat{x}$ ), is looking from near the midpoint of the domain in  $x$ , the top of the domain (looking down) in  $z$ , and the edge of the domain in  $y$ . The billow (not shown) would be centered in the bottom left corner of the image.

## 5.4 Secondary Instabilities

In the 3D DNS case we observed several secondary instabilities including the formation of a pair of vortex structures downstream from the billow and convective plumes on the periphery of the billow. Similar secondary instabilities are illustrated by Thorpe in Fig. 1b as observed in laboratory experiments. The vortex structures shown in Fig. 11 occur at the edge of the billow structure, just downstream from the billow's core. As can be seen in the coloring of the field lines, the vortices have large values of streamwise vorticity in their cores, but not larger than the much smaller scales seen in the strong red and blue patches along streamlines in other regions of the domain. Coloring these streamlines with the total temperature (including the linear background gradient) shows that they are not convectively driven but are rather the result of a strong vortex stretching effect. They are formed when a small-scale vortex escapes the turbulent region of the billow and enters the layer of strong shear above the billow. The

small-scale vortex is then aligned with the flow and stretched by the strong downstream flow above the billow, forming one of the vortices pictured in Fig. 11. This vortex pair is short lived and is disrupted as the billow expands in the  $x$  direction until being completely shredded by turbulence by  $t = 80$ .

We also observed a secondary convective instability in our simulation using volume renderings of both total temperature and cross-stream velocity. The convective instability, shown in Fig. 12, consists of two up-welling plumes of hot fluid moving through a region of cooler fluid behind the core of the Kelvin-Helmholtz billow. This instability, like the vortex pair, is driven by the strong shear at the edge of the billow. In this case, hot fluid from the well-mixed core of the billow is pulled downstream on the bottom of the billow into the still stratified region in the tail of the billow. Since this fluid is hotter than its surroundings it forms a pair of plumes, which can be seen in Figs. 9c and 9d with the characteristic “mushroom” shape at the tops of the plumes. As with the vortex pairs, this instability is short lived as the turbulence in the core quickly expands in the  $x$  direction to fill the domain in the  $x$  and  $y$  directions.

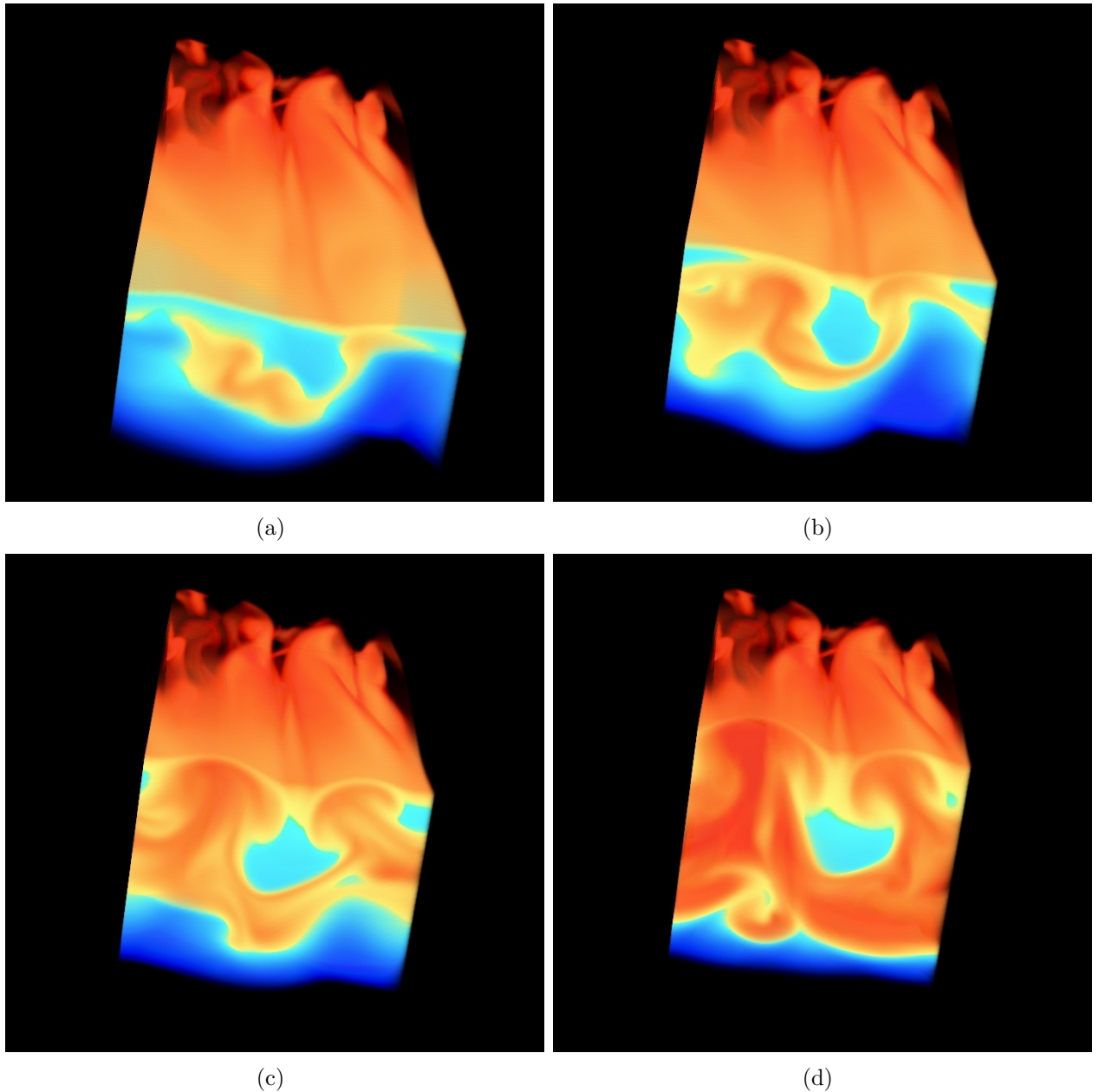


Figure 12: Volume visualization of total temperature with blue as cold and red as hot fluid, showing convective plumes in the 3D DNS case. Viewpoint is looking upstream (in the  $x$  direction) from downstream of the billow with a slight  $15^\circ$  tilt in the  $y$ - $z$  plane. Moving from (a) to (d) we have progressively cut further into the domain to show the convective plumes as a function of  $x$ . The frames show (a) the full domain, (b) 93%, (c) 87%, and (d) 81% of the domain. For reference, the vortex pair shown in Fig. 11 would sit almost directly above the plumes in (b) and (c), but end before the cut-away depth in (d).

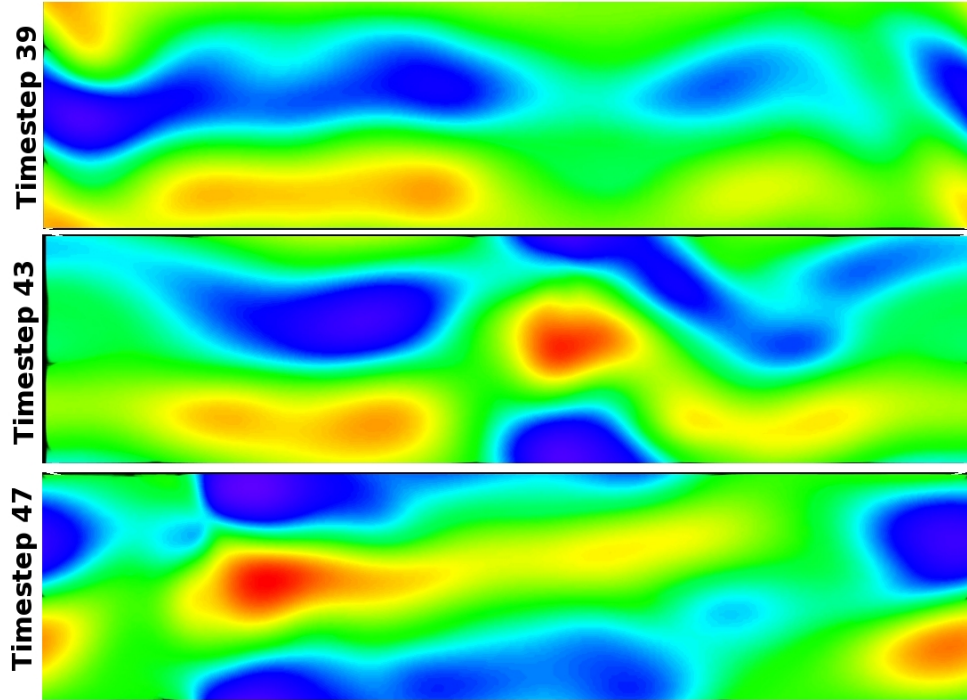


Figure 13: Volume visualization of  $y$  velocities in the  $x$ - $y$  plane directly above the billow, with positive values of  $v$  in blues and negative values in reds.

The convective instability can also be seen on the top and bottom of the billow. Figure 13 is a visualization of the convective roll instability illustrated by Thrope in Fig. 1 in cross-stream velocity  $v$ . The streamlines flowing over the billow are susceptible to convective instability. In Fig. 13, we are looking down onto the top of the billow. The main flows are in  $x$  direction, from left to right in the figure. The  $y$  velocities are two orders of magnitude smaller than the dominant flow. However, the coherent structures seen in Fig. 13 are likely a signature of the convective secondary instability. Red and blue mark large negative and positive velocity respectively. The green horizontal channels represent the sides of the convective cells where the circulation is predominantly in the  $z$  direction. The red and blue channels mark the crests of the cells where the velocity is predominantly in the  $y$  direction. The fact that these velocity structures are banded is a consequence of the instability occurring *along* streamlines. Although the streamlines are mostly horizontal (maintaining at constant  $y$ ), it is clear that wave-like fluctuation can occur in the  $y$  direction, as is seen in time-step 43 in Fig. 13. Kinking of the streamlines might contribute to the vortex pairs we observe because it places streamlines in nearly intersecting routes. This small scale intersection is likely an analog of billow-billow knots which have been reported in laboratory experiments (see Fig. 1).

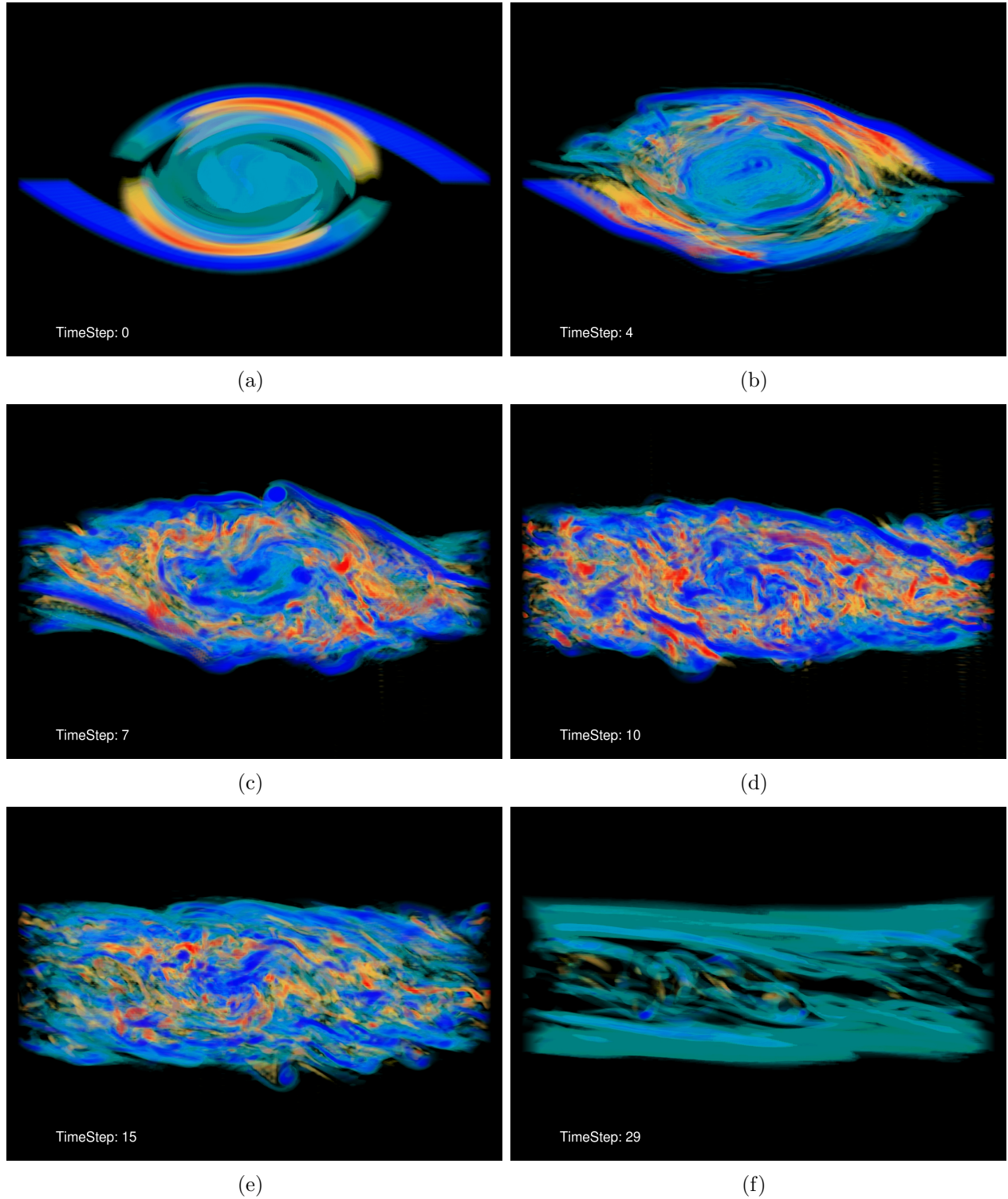


Figure 14: Volume renderings of the  $y$ -component of vorticity at various times during the 3D LES case where color goes from reds and yellows (negative values of  $\omega_y$ ) to greens and blues (positive values). Note that this figure uses the same transfer function as Fig. 6 but has fewer points in the  $y$  direction, which causes a more transparent look. This figure also uses the same times for each frame as in Fig. 6.

## 6 Large Eddy Simulation

The time evolution of the LES case in  $\omega_y$  is shown in Fig. 14. When compared with the time evolution of the DNS case, there is surprising agreement between the two models despite a factor of three less resolution in all directions for the LES case. At early times it is even possible to identify common medium-scale features in the DNS and LES vorticity images (see Figs. 6b and 14b, for example). In Fig. 14, the lower resolution has, however, made the solutions look less well resolved and careful inspection reveals large amounts of ringing in the interior of the billow due to low resolution, especially in the  $x$  direction.

The spectra for the LES case exhibits much of the same behavior as the spectra for the DNS case, as shown in Fig. 15. The LES spectra closely follows the spectra for the 3D DNS case even at later times. There is an odd bump in the LES spectra at  $k \approx 65$  and  $t = 44$  that is not present in the DNS case. This could simply be an oddity of the spectra at those particular times as these spectra are not averaged in time.

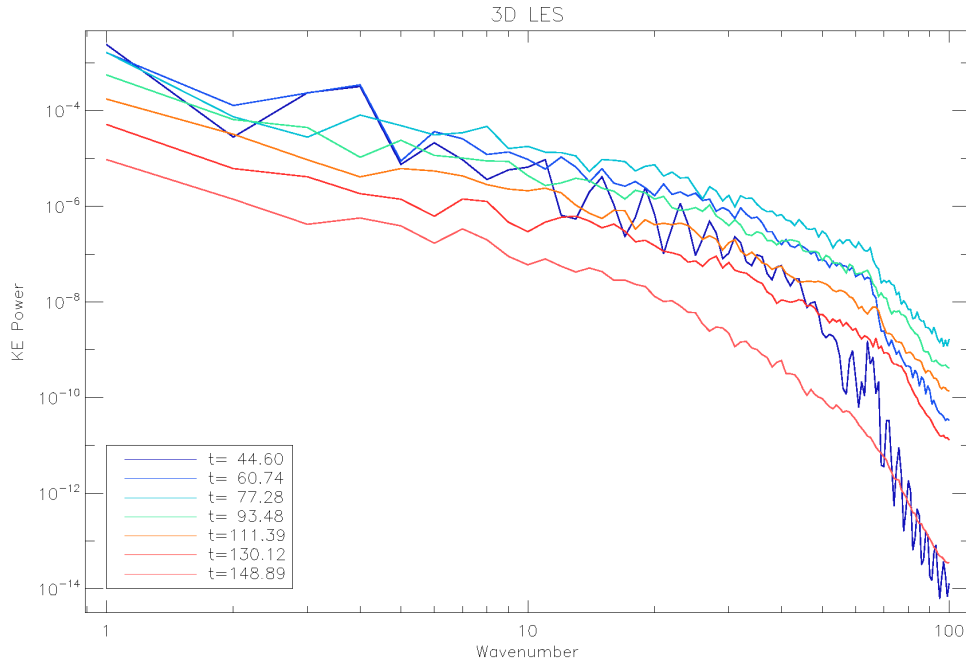


Figure 15: Spectra in the  $x$  direction at the mid-plane, averaged over the  $y$  direction at a single instant in time for (a) the LES case and (b) comparing the DNS, LES, and 2D cases. In (b) the spectra at  $t = 93$  and  $t = 148$  are offset by factors of  $10^3$  and  $10^6$  respectively for visual clarity.

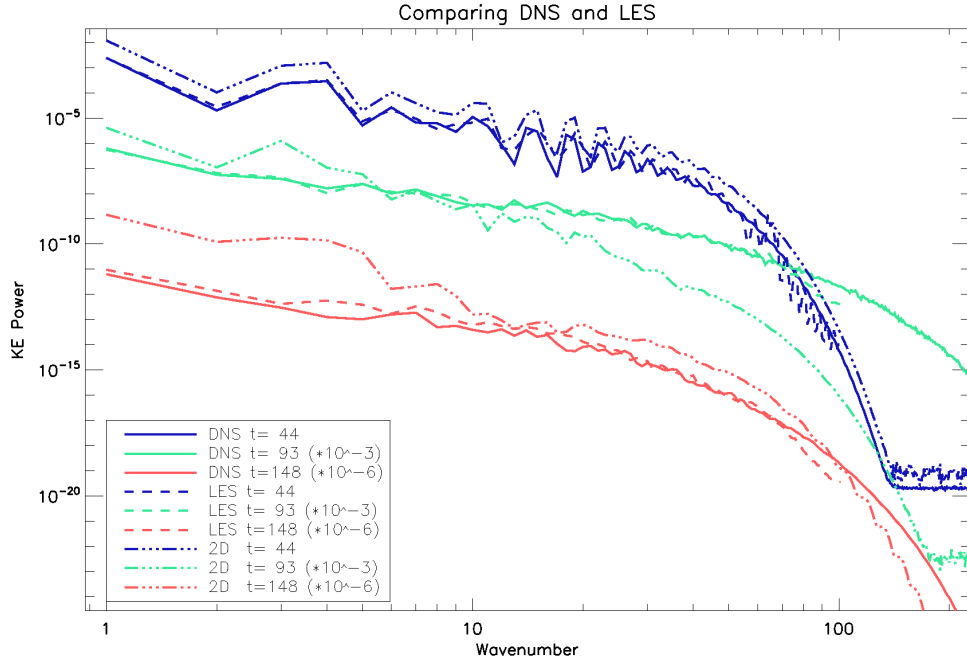


Figure 16: Spectra in the  $x$  direction at the mid-plane, averaged over the  $y$  direction at a single instant in time comparing the DNS, LES, and 2D cases. The spectra at  $t = 93$  and  $t = 148$  are offset by factors of  $10^3$  and  $10^6$  respectively for visual clarity.

## 7 Conclusions

Comparing the three cases we ran with  $Ri = 0.1$ , we can make several conclusions. First, from the qualitative descriptions of the time evolution of the 2D (see Fig. 4), 3D DNS (see Fig. 6), and 3D LES cases, we can immediately see that the 2D case does accurately represent the 3D behavior of this system. If we compare the spectra of the three cases, as done at three times in Fig. 16, it is obvious that the 2D spectra has far too much power in the low  $k$  modes at late times and far too little power in the high  $k$  modes during the turbulent phase. This is a result of the fact that in 2D turbulence there is not vortex stretching or turning mechanism, which inhibits the development of a turbulent cascade and allows for an inverse cascade, which in our system has piled up two orders of magnitude more kinetic energy at the largest scales than either of the 3D cases at late times.

We can also compare some of our results quantitatively with those of the other two groups,  $\alpha$  and  $\sigma$ . Our Richardson number was an intermediate value, between that of the other two groups, so as expected our dynamics were quantitatively intermediate between the other two groups. In the 3D DNS simulations, we developed turbulence along the edge of the billow that worked its way inward to the core in a manner similar to group  $\alpha$ , however our core became turbulent much faster than theirs. The turbulent region in our 3D DNS case also remained strongly confined in  $z$  in a manner similar to that of group  $\sigma$ , but did not develop the strong enstrophy “tubes” on the edges of the turbulent region seen in their 3D volume visualizations. In our analysis, our case fell into the generally expected state of being intermediate between cases  $\alpha$  and  $\sigma$ .